

## MarsGT: Multi-omics analysis for rare population inference using single-cell graph transformer

Xiaoying Wang<sup>1,2,\*</sup>, Maoteng Duan<sup>3,\*</sup>, Jingxian Li<sup>3</sup>, Anjun Ma<sup>1,2</sup>, Dong Xu<sup>4,5</sup>, Zihai Li<sup>2</sup>,  
Bingqiang Liu<sup>3,§</sup>, Qin Ma<sup>1,2,§</sup>

<sup>1</sup> Department of Biomedical Informatics, College of Medicine, The Ohio State University, Columbus, OH, 43210, USA

<sup>2</sup> Pelotonia Institute for Immuno-Oncology, The James Comprehensive Cancer Center, The Ohio State University, Columbus, OH 43210, USA

<sup>3</sup> School of Mathematics, Shandong University, Jinan, Shandong, 250100, China

<sup>4</sup> Department of Electrical Engineering and Computer Science, University of Missouri, Columbia, MO 65211, USA

<sup>5</sup> Christopher S. Bond Life Sciences Center, University of Missouri, Columbia, MO 65211, USA

\* These authors contributed equally

§ These authors jointly supervised this work:

Bingqiang Liu: [bingqiang@sdu.edu.cn](mailto:bingqiang@sdu.edu.cn)

Qin Ma: [qin.ma@osumc.edu](mailto:qin.ma@osumc.edu)

### Abstract

Rare cell populations are key in neoplastic progression and therapeutic response, offering potential intervention targets. However, their computational identification and analysis often lag behind major cell types. To fill this gap, we introduced MarsGT: Multi-omics Analysis for Rare population inference using Single-cell Graph Transformer. It identifies rare cell populations using a probability-based heterogeneous graph transformer on single-cell multi-omics data. MarsGT outperformed existing tools in identifying rare cells across 400 simulated and four real human datasets. In mouse retina data, it revealed unique subpopulations of rare bipolar cells and a Müller glia cell subpopulation. In human lymph node data, MarsGT detected an intermediate B cell population potentially acting as lymphoma precursors. In human melanoma data, it identified a rare MAIT-like population impacted by a high IFN-I response and revealed the mechanism of immunotherapy. Hence, MarsGT offers biological insights and suggests potential strategies for early detection and therapeutic intervention of disease.

Multicellular organisms encompass a diverse range of specialized cells. Identifying these cell types is pivotal in immunotherapy and clinical scenarios, as it illuminates immune mechanisms, aids in devising targeted therapies, and bolsters personalized medicine by unmasking the unique cellular makeup of each patient<sup>1</sup>. However, difficulties surface when encountering rare or transiently expressed cells<sup>2,3</sup>. Despite their scarcity, rare cell populations step up to play crucial roles in a variety of biological processes<sup>4,5</sup>. For example, antigen-specific memory T cells are integral for sustained immunosurveillance and long-term immunity, even in infection-free periods<sup>6</sup>. Conversely, invariant natural killer T cells impact a variety of pathologies, including microbial infections and autoimmune diseases, due to their robust immunoregulatory functions<sup>7,8</sup>. Additionally, minimal residual disease, denoting the minute cancer cell population post-treatment, acts as a significant early indicator for potential tumor relapse, highlighting the necessity to identify and comprehend these rare cell groups in disease dynamics and therapeutic interventions<sup>9,10</sup>. A refined grasp of these rare cell populations, culminating in a more detailed depiction, will illuminate our understanding of tumor microenvironments and the intricate mechanisms that steer the responses to immunotherapy.

The advent of single-cell RNA sequencing (scRNA-seq) has vastly improved our ability to identify individual cell types, offering high-resolution molecular profiles that illuminate cellular diversity and the complex dynamics of gene expression within specific cells<sup>11,12</sup>. Most existing rare cell identification tools, such as FIRE<sup>4</sup>, GapClust<sup>13</sup>, TooManyCells<sup>14</sup>, GiniClust<sup>15</sup>, RaceID<sup>2</sup>, and SCMER<sup>1</sup>, confront several challenges, such as high false positives when inferring rare populations, limited performance with complex samples like tumor biopsy single-cell data, inability to concurrently identify major and rare cell types, and compromised accuracy with ultra-rare cell types (<1% of the sample). These issues could stem from the limited representation of rare cells, which may lead to inaccurate grouping with more prevalent cell populations when solely relying on gene expression data. This pursuit can be further accelerated by technological innovations like single-cell ATAC sequencing (scATAC-seq)<sup>12</sup>. When synergistically used with scRNA-seq, these methodologies provide partial regulatory data concerning enhancer regions pivotal in preserving cell type identities<sup>1</sup>. This invaluable information can be tapped into for the construction of gene regulatory networks, thereby unraveling critical insights into the nature and function of rare cell populations<sup>16</sup>.

Meanwhile, graph neural networks have recently demonstrated profound proficiency in deciphering complex biological data, offering robust backing for the precise analysis and study of scMulti-omics data<sup>16-20</sup>. The implementation of the heterogeneous graph transformer provides a unified framework that amalgamates diverse single-cell data types, thereby facilitating a comprehensive understanding of cellular heterogeneity<sup>16,21-23</sup>. This approach unveils the intricate interplay among various cell types within complex cellular landscapes, enhancing our comprehension of biological systems and bolstering opportunities for precision therapeutic interventions.

To fill the gap and validate the theory, we developed MarsGT (**M**ulti-omics analysis for rare population inference using **s**ingle-cell **G**raph **T**ransformer), an end-to-end deep learning model for rare cell population identification from scMulti-omics data. Graph neural networks have recently demonstrated profound proficiency in modeling single-cell data<sup>24,25</sup>. Furthermore, our in-house tool, DeepMAPS<sup>16</sup>, has shown the superior performance of heterogeneous graph transformer (HGT), a powerful graph neural network architecture that can deal with large-scale heterogeneous and dynamic graphs, in biological network inference and cell clustering from the joint analysis of scMulti-omics data. With such a foundation, MarsGT introduces a probability-based HGT framework to analyze scMulti-omics data from a heterogeneous graph, including cells, genes, and peaks, which can build peak-gene regulatory relationships and utilize such relationships to characterize rare cell populations.

MarsGT, as a novel probability-based subgraph-sampling method, can highlight rare cell-related genes and peaks in a heterogeneous graph. We conducted extensive simulations (n=400) to thoroughly test the accuracy and robustness of MarsGT in identifying rare cell populations. The performance of MarsGT, validated on the above simulation data and four human peripheral blood mononuclear cell datasets, surpassed existing methods in F1 score and Normalized Mutual Information (NMI) metrics. To further showcase the application capability of MarsGT, we applied MarsGT on three scMulti-omics case studies of (1) mouse retina, (2) human Fresh Frozen Lymph Node with lymphocytic lymphoma, and (3) melanoma patients and healthy donors. Our results demonstrate that MarsGT can distinguish unique rare cell populations—a feat not achievable with other computational tools—and provide strategies for early clinical detection and the development of immunological blockers.

## Results

### ***Overview of the MarsGT framework***

MarsGT incorporates scRNA-seq and scATAC-seq data, and concurrently yields primary and rare cell populations along with their respective regulatory relations (**Fig. 1, Supplementary Fig. 1**). A heterogeneous graph, comprising cells, genes, and enhancers, is constructed from the initial scRNA-seq and scATAC-seq data, with the presence of genes and peaks within cells represented as edges. The genes/peaks within a cell are segmented into high or low-selection regions according to the first quartile of the expression/accessibility. For a given cell, the selection probability of a gene/peak is determined by the proportion of gene/peak expression/accessibility in the high selection region. With the selection gene/peaks criteria, subsampling graphs are specifically tailored for rare cells. The multi-head attention mechanism facilitates the update of joint embeddings of cells, genes, and peaks on the sampled subgraphs. The cell assignment probability matrix and peak-gene link assignment probability matrix are predicted post-learning joint embedding. The peak-gene relations and rare cell populations from the subgraphs are concurrently determined and iteratively updated for model training. The fully trained model is subsequently applied to the entire heterogeneous graph, and a transcription factor (TF) database is incorporated to

construct cell cluster enhancer gene regulatory networks (eGRNs)<sup>12</sup> (**Methods**).

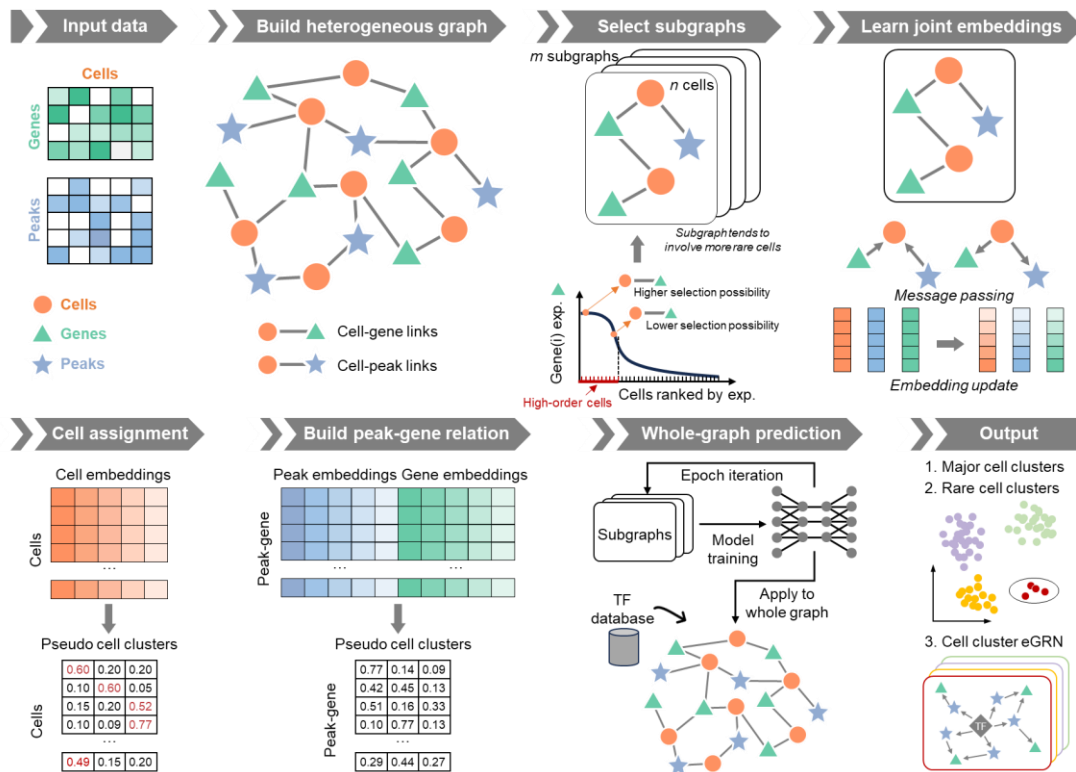


**Fig. 1. The framework of MarsGT.** The model employs a six-step process for cell clustering and eGRN inference from matched scRNA-seq and scATAC-seq data. First, a heterogeneous graph, comprised of cells, genes, and peaks, is constructed from the original scRNA-seq and scATAC-seq data. Genes and peaks serving as edges are selected for a cell if they show high accessibility/expression within that cell and low accessibility/expression in others. The second step is learning joint embedding, which employs four graph relations to pass the message via a heterogeneous transformer. Arrows depict connections between target and source nodes. The third step involves cell assignment. Here, cell clusters are inferred from a probability matrix with rows representing cells and columns indicating pseudo-cell clusters. Cells that share the same maximum probability belong to the same cluster. The fourth step is constructing the peak-gene relationship via a matrix calculated from gene and peak embeddings, with rows denoting the regulatory potential of the peak to gene and columns indicating pseudo-cell clusters. In the final step, the trained model is applied to the entire graph. Following this, TF database information is integrated to infer cell clusters and eGRNs. Circles represent rare cell populations.

***MarsGT achieves superior performances in rare and major cell populations identification simultaneously on simulated and real data***

We assessed the performance of MarsGT in identifying both rare and major cell populations across 400 simulated matched scRNA-seq and scATAC-seq datasets. To evaluate the performance of tools on distinct datasets. We simulated 100 datasets using highly homogeneous cell line data (Sim-CL 1, 2). To test these tools in more complex, less distinguishable scenarios, we simulated an additional 300 datasets using peripheral blood mononuclear cell (PBMC) data (Sim-PBMC 1, 2, 3, 4, 5, 6)

**(Supplementary Data 1, Methods)**. Each simulated dataset included benchmark annotations from their original manuscripts. MarsGT was first compared with CellCUIIS<sup>26</sup>, FIRE<sup>4</sup>, and GapClust<sup>15</sup>, which operate as classification-like tools, to infer rare cells only. The performance was evaluated based on the F1 score, Precision, and Recall metrics for rare cell identification performance. To ensure fairness, each benchmarking tool was also tuned with different parameter combinations **(Methods)**. We selected the parameter combination for performance comparison based on the grid search benchmarking of all the above tools. Specifically, if the mean score of a parameter combination achieves the highest across all datasets, we consider it the default parameter **(Methods)**. MarsGT outperformed all classification-like tools across seven types of simulated datasets (totaling 350) regarding F1 score, Precision, and Recall **(Fig. 2a, Supplementary Fig. 2, Supplementary Data 2)**.

Furthermore, to evaluate MarsGT's ability to identify major and rare cell populations simultaneously, we compared it with three clustering-like tools (GiniClust<sup>13</sup>, RaceID<sup>2</sup>, and SCMER<sup>1</sup>) using NMI, Purity, and Entropy metrics. MarsGT was 5.66% higher than the NMI score of the existing best-performing tool on the independent test dataset **(Fig. 2b, Supplementary Fig. 3, Supplementary Data 2)**. Furthermore, to verify MarsGT's rate of false positives, we compared it with other tools using the Sim-PBMC 6 dataset, which lacks rare cells **(Methods)**. The results confirm that MarsGT does not force the identification of rare cell populations **(Supplementary Fig. 4, Supplementary Data 3)**. A cell type is classified as a rare cell type if it constitutes less than 3% of the total cells. However, certain rare cells, such as senescent cells, can constitute an even smaller proportion<sup>27</sup>. To assess each tool's ability to identify these extremely rare cell types, we performed a gradient test with proportions of 0.5%, 1%, 2%, and 3% rare cells across five simulated datasets. A detailed comparison across all evaluation metrics demonstrated that MarsGT outperformed the existing top-performing tool in rare cell identification, exhibiting a superior F1 score that was 11.56%~143.49% higher, across different proportions of rare cells **(Supplementary Fig. 5, Supplementary Data 4)**.

To evaluate MarsGT's performance on real datasets, we chose four datasets (PBMC-bench-1, 2, 3, and PBMC-test) from human peripheral blood mononuclear cells with ground truth labels. To maintain fairness, we presented the performance in a bar plot, using default parameters for all benchmarking tools and showing the results of parameter combinations **(Supplementary Data 5-6)**. In real data, we separately classified cell types constituting less than 3% and 1% of total cell counts as rare cell types. On average, MarsGT achieved 13.21% and 64.08% higher F1 scores, compared to other tools, for 1% and 3% simulated rare cell proportion identification, respectively **(Fig. 2c)**. The cell clustering UMAP on an independent dataset with benchmarking labels illustrated that MarsGT can accurately identify all rare cell types compared to other tools **(Fig. 2d)**. The cell clustering UMAP on an independent dataset with benchmarking labels illustrated that MarsGT can accurately identify all rare cell types compared to other tools **(Supplementary Fig. 6, Supplementary Data 7)**, which confirmed MarsGT's robust stability.

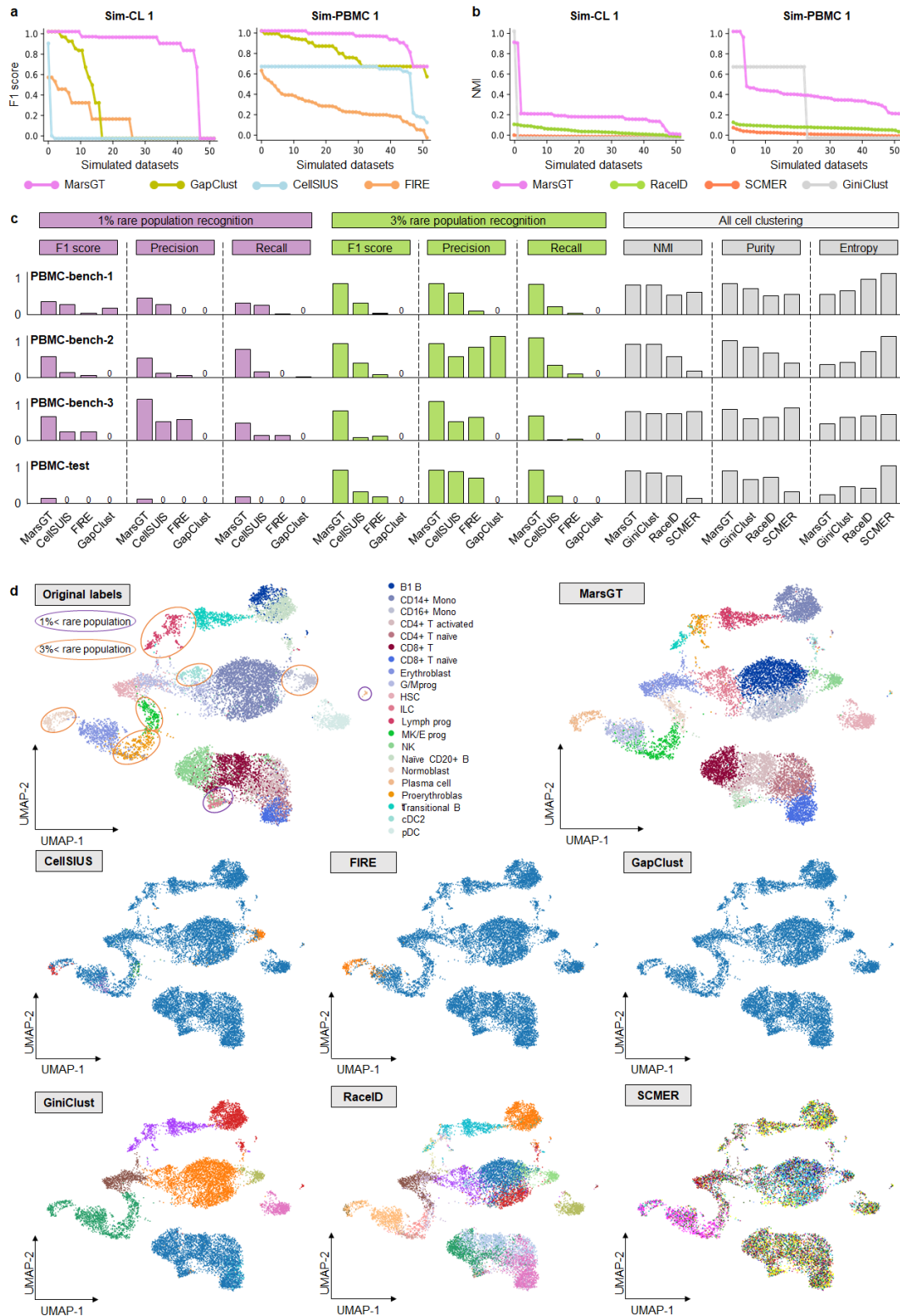


**Fig. 2. Benchmarking of MarsGT in terms of rare cell population identification. a.** Benchmark rare cell population identification on Sim-CL 1 and Sim-PBMC 1 datasets with classification-like tools in terms of F1 score. The X-axis signifies the dataset, while the Y-axis presents F1 scores arranged in descending order. **b.** Rare cell population identification on Sim-CL 1 and Sim-PBMC 1 datasets benchmarked with clustering-like tools evaluated via NMI scores. The X-axis signifies the dataset, while the Y-axis denotes NMIs, organized in

descending order. **c.** Comparative results on three real training datasets (PBMC-bench-1, 2, 3) and one independent test dataset (PBMC-test). Test parameters across all tools are determined by the most optimal results obtained from the training dataset. **d.** The UMAPS results for the independent PBMC-test dataset were calculated using PCA and predicted cell clusters in the tools. The purple and orange ellipses represent rare cell populations constituting less than 1% and 3%, respectively. Tools like FIRE and GapClust can distinguish only between major and rare populations in a binary fashion based on their method design. CellSISU, due to its design, can identify several rare cell populations but cannot recognize major ones.

***MarsGT effectively captures differential regulatory mechanisms and uncovers biologically meaningful rare cell populations often missed by other tools.***

To underscore MarsGT's robust capability in identifying rare cell populations within species beyond humans, we utilized MarsGT on a published dataset involving matched single-nucleus RNA sequencing (snRNA-seq) and single-nucleus ATAC sequencing (snATAC-seq) performed on 9,383 cells from the mouse retina (**Supplementary Data 1**). This study demonstrates MarsGT's capabilities in discerning major and numerous rare cell populations, and we were able to identify 18 distinct cellular clusters, inclusive of one amacrine cell (AC) group, eight bipolar cell (BC) groups, one Cone cell group, one horizontal cell (HC) group, three müller glia cell (MG) groups, one retinal ganglion cell (RGC) group, and three Rod cell groups (**Fig. 3a**). Moreover, 12 rare cellular populations were distinguished, eight of which boast a 95% confidence level as highlighted by scPower<sup>28</sup> (**Fig. 3b**). The annotation of major cell populations was accomplished through the visualization of expression levels pertaining to curated marker genes<sup>29-31</sup> (**Fig. 3c**). The populations of BC are known to exhibit a multitude of rare populations. Utilizing MarsGT, we identified eight unique populations of BC. These populations were annotated by visualizing the expression levels of curated marker genes specific to the BC subpopulation<sup>32</sup> (**Fig. 3d**). Excluding rod bipolar cell (RBC), all eight populations are regarded as rare cell populations at a 95% confidence level, as determined by scPower<sup>28</sup>.

To validate whether the rare cell populations we identified is a false positive, further testing is required. Hence, we inferred potential cell-cell communications and constructed communication networks among different BC populations using CellChat<sup>33</sup>. Notably, we identified a non-canonical Wnt (ncWnt) signaling pathway originating from RBC and targeting both BC3 and BC6 (**Supplementary Fig. 7, Supplementary Data 8**). Previous research has highlighted the role of Wnt5a and Wnt5b, produced by RBC, in activating a non-canonical signaling pathway in rods, which in turn regulates early Outer Plexiform Layer (OPL) patterning<sup>34</sup>, thereby validating the accuracy of the rare cell populations identified by MarsGT. We calculated the differentially expressed genes (DEGs) for each population further to elucidate the functionality of these distinct BC populations. Based on the cell population-specific DEG list, we inferred the functional pathways for each cell population (**Fig. 3e**). Notably, neuron migration was moderately enriched in BC1B, which aligns with its translocation from the bipolar to the amacrine cell layer. Categories such as axonogenesis and the glutamate receptor signaling

pathway revealed modest differences among BC clusters. Interestingly, extracellular ligand-gated ion channel activity was predominantly enriched in OFF types, reflecting their employment of ionotropic glutamate receptors<sup>35</sup>.

Interestingly, our analysis distinguished cluster 10, which comprises 127 cells, from cluster 2. Although both clusters are annotated as MG, cluster 10 stands out as a rare cell population. We denote cluster 2 as MG-1 and cluster 10 as MG-2. In the original paper, the 127 cells are annotated as Rod (120) and MG (5) by scRNA-seq and marker gene<sup>36</sup>. To further validate our findings, we utilized GiniClust<sup>15</sup>, the algorithm with the second-best performance in our benchmarking section after MarsGT. GiniClust annotated the 127 cells as Rod (83 cells) and MG (41 cells) (**Supplementary Fig. 8**). This indicates that the rare MG identified in our study, which was not found in the original text, are not false positives. We ventured further into exploring the functional differences between the two MG clusters. Notably, we found MG-1 to be enriched in sprouting angiogenesis (**Fig. 3f**), suggestive of potential defects in retinal vascular development and a consequential functional deficit in MG, known to play a critical role in guiding outgrowing vessels<sup>37</sup>. MG-2 exhibited enrichment in the structural constituent of eye lens function (**Fig. 3f**). This finding echoes the assertions of previous research indicating that MG in both mature and embryonic retina binds antibodies generated to a lens fraction enriched for  $\alpha$ -crystallin, a key lens protein<sup>38</sup>. The eGRN of the structural constituent of eye lens pathway related-gene is displayed in **Supplementary Fig. 9 (Supplementary Data 9)**. We further visualized the eGRN for MG-1 and MG-2 (**Fig. 3g, Supplementary Data 10**). Compared to other methods, MarsGT effectively captures differential regulatory networks, successfully identifying biologically meaningful rare cell populations that are often missed by RNA-only or other tools.

To further assert that MarsGT does not overlook pertinent information in the data while identifying rare cell populations, we initially compute the differentially expressed genes of the predominant cell populations. We identified top DEGs such as *Arr3*, *Gnat2*, and *Pde6h*, which act as marker genes for the Cone. Additionally, *hsd7a* serves as the marker gene for HC, whereas *Apoe*, *Clu*, and *Slc1a* function as marker genes for MG. *Meg3* is identified as the marker gene for RGC, and *Nrl* for Rod<sup>32</sup> (**Supplementary Fig. 10, Supplementary Data 11**). The results validate the accuracy of MarsGT in identifying the predominant cell populations. Utilizing the raw gene expression data and cell populations, we deduced potential cell-cell communications and subsequently constructed communication networks among different cell populations within multiple signaling pathways, facilitated by CellChat<sup>33</sup>. Notably, we discovered a VEGF signaling pathway extending from AC, MG, RGC, HC, MG, and Rod towards MG as the target (**Supplementary Fig. 11, Supplementary Data 12**), which is consistent with the previous research<sup>30</sup>.



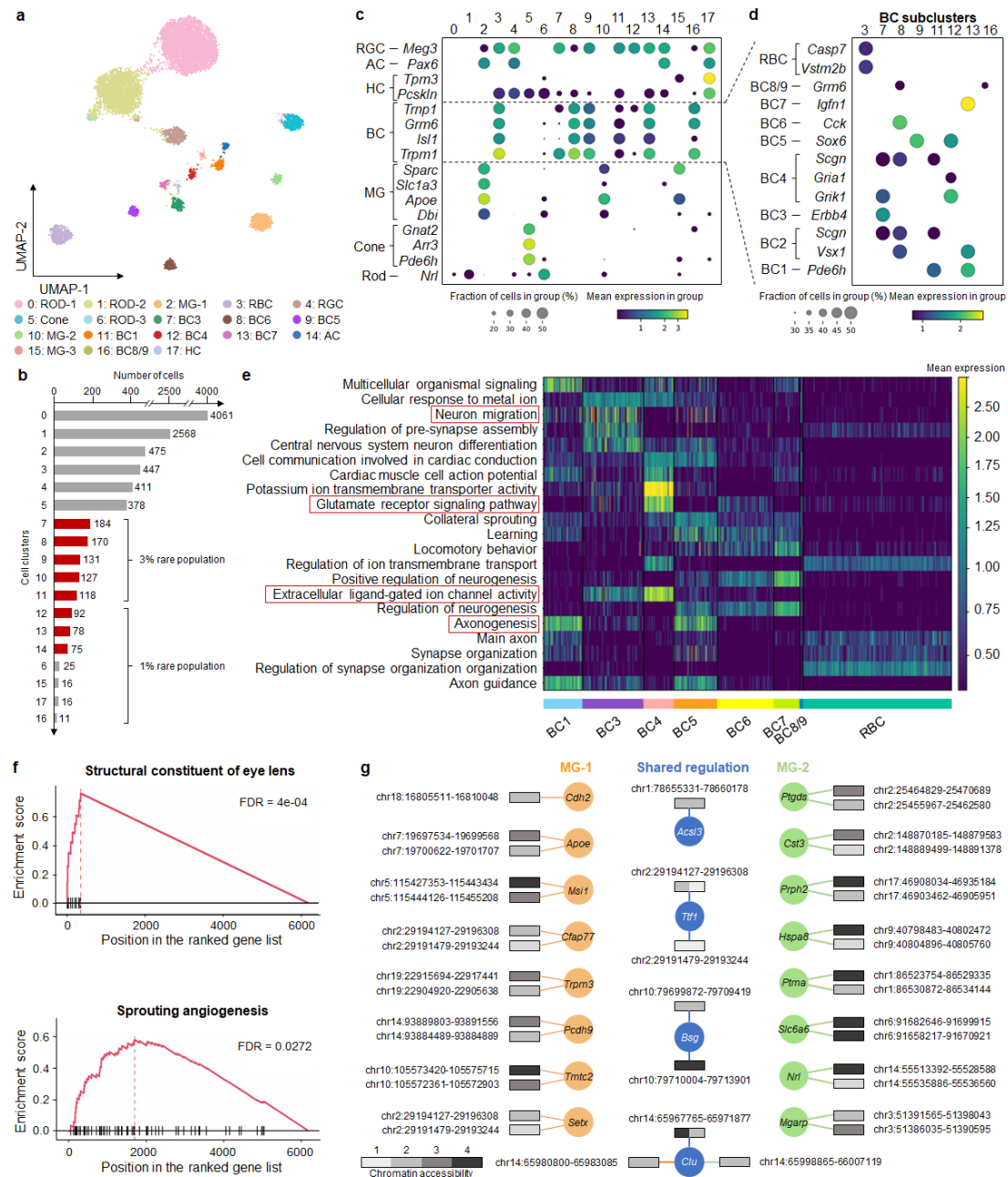


**Fig. 3. MarsGT effectively captures differential regulatory mechanisms and uncovers biologically meaningful rare cell populations often missed by other tools. a.** A UMAP visualizing the cell clusters predicted by MarsGT, annotated based on marker genes. **b.** The number of cells in each cell cluster, with the red color signifying a 95% confidence level for rare cell populations. **c.** Dotplot depicts the expression value and proportion of marker genes for the cell clusters predicted by MarsGT. **d.** Dotplot represents the expression value and proportion of BC marker genes for the cell clusters predicted by MarsGT. **e.** The average gene expression across each pathway is calculated using differentially expressed genes (DEGs) across various BC subpopulations. Pathways within the red box have been validated in the literature. **f.** Pathway enrichment as determined by Gene Set Enrichment Analysis (GSEA), based on the DEGs of MG-1 and MG-2. The structural constituent of the eye lens is the pathway enriched in MG-2, and Sprouting angiogenesis is the pathway enriched in MG-1. **g.** The different peak-

gene networks of MG-1 and MG-2. Rectangles symbolize the peaks, and their colors represent the mean accessibility of the peak in the cell population. Accessibility levels ranging from 0 to 0.1 are denoted as 1, those from 0.1 to 0.5 as 2, from 0.5 to 1 as 3, and anything above 1 is denoted as 4. The color of the line and circle represent the cell populations. The orange color signifies genes or relationships unique to MG-1, green indicates those unique to MG-2, while blue represents genes or relationships shared between MG-1 and MG-2.

### ***MarsGT identifies rare B lymphoma-state-1 that provide the potential for preventing B-lymphoma progression***

To underscore MarsGT's robust capability in identifying rare cell populations within cancer data, we utilized a matched scRNA-seq and scATAC-seq dataset available on the 10X Genomics website (**Supplementary Data 1**). This data originated from 14,566 cells obtained from a flash-frozen intra-abdominal lymph node tumor in a patient diagnosed with diffuse small lymphocytic lymphoma of the lymph node. MarsGT identified 14 distinct cell clusters, which we annotated by visualizing the expression levels of curated marker genes (**Fig. 4a, b**). Notably, four of these clusters were annotated as B cells. To differentiate the subpopulations of B cells, we visualized the expression levels of both normal B marker genes and B lymphoma marker genes across the four subpopulations (**Fig. 4c**). We designated one subpopulation as normal B cell population and three as lymphoma cell populations: B lymphoma-1 (Bsl1), B lymphoma-2 (Bsl2), and B lymphoma-3 (Bsl3). Bsl1, a rare cell population, exhibits a 95% confidence level, as indicated by scPower<sup>28</sup>. Intriguingly, it was evident that B cell subpopulations annotated using solely RNA or ATAC data could not be effectively distinguished (**Fig. 4c, Supplementary Fig. 12**). We also applied other scMulti-omics tools to the dataset for comparative purposes. For instance, Seurat<sup>39</sup> only identified two B cell subpopulations with hard annotation by curated marker genes (**Supplementary Fig. 13**), while our in-house tool DeepMAPS identified only three B cell subpopulations<sup>16</sup>. However, neither tool successfully identified the rare cell cluster within the B cells.

A pseudotime analysis on the four B cell clusters (comprising the normal B cell populations and three B lymphoma cell populations), using Monocle3<sup>40</sup>, postulated a lineage whereby the rare cell population Bsl1 originates from the normal B cell populations. It was inferred that Bsl1 predates Bsl2, which in turn predates Bsl3 (**Fig. 4d, e**). To substantiate this proposed linear-like developmental trajectory, we computed gene signature scores<sup>41</sup> reflecting different functions (anti-apoptosis, metastatic, and PD-PDL1) across the four B cell populations (**Fig. 4f, Supplementary Data 14, Supplementary Data 15**). These results depict a progressive progression of B lymphoma from Bsl1 to Bsl3. Focusing on PDL1, a critical gene in the PD1-PDL1 pathway that is promoted by STAT1 and HIF1A, we observed more regulatory relations and intensity of STAT1 and HIF1A in Bsl3 (**Fig. 4g, h, Supplementary Data 16**). This finding is in line with our inferred linear-like development tendency. Furthermore, BCL2, an oncogenic gene that plays an anti-apoptotic role in cancer and drives its progression<sup>42-45</sup>, demonstrated an incrementally enhanced regulatory score from

normal B cells to Bsl3 (**Fig. 4i, Supplementary Data 17**), lending further credibility to our inference. Exploring Bsl1 in greater depth, we compared the disparities among the four B cell clusters and identified a unique TF for Bsl1, namely, *MEF2C*, along with switch-enhancer corresponding TFs: *POU2F2*, *FOXP1*, *SPI1*, and *NFIC*. Simulating a knockout experiment<sup>46</sup> involving these five TFs revealed a shift in B lymphoma cells towards normal B cells, suggesting that identifying the rare Bsl1 state could offer potential avenues for curbing B-lymphoma progression (**Fig. 4j, k, Supplementary Fig. 14**). It has been reported previously that *MEF2C* mutations lead to deregulated expression of the *BCL6* oncogene in B lymphoma<sup>47,48</sup>, and that *POU2F2* reflects the survival of B cell malignancies<sup>49</sup>. Additionally, *FOXP1* is known to suppress immune response<sup>50-53</sup>. The roles of *SPI1* and *NFIC*, as inferred by MarsGT, may provide fresh insights into therapeutic strategies for B lymphoma. In short, MarsGT can effectively identify a rare subset of B cells, Bsl1, provides valuable insights into B-lymphoma progression, and opens new avenues for potential interventions, thereby advancing our understanding of cellular disease dynamics and fostering innovative medical research and treatment strategies.

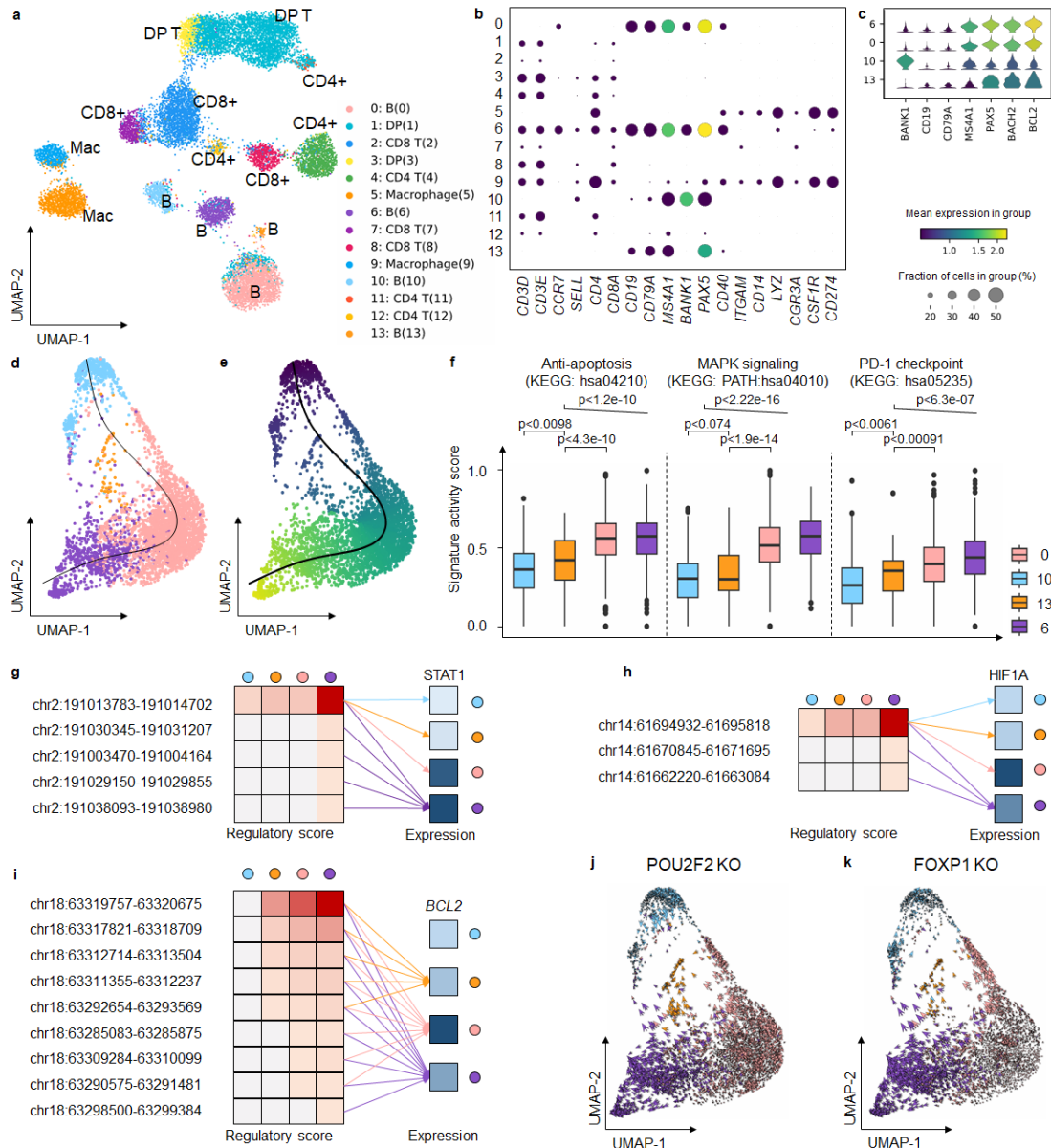


**Fig. 4. MarsGT identifies the rare cells in the intermediate transition state on B lymphoma data.** **a.** UMAP visualizes cell clusters predicted by MarsGT, annotated based on the marker genes. **b.** Dotplot demonstrates the expression value and proportion of marker genes within the cell clusters predicted by MarsGT. **c.** A stacked violin plot represents the subpopulations of B cells, annotated with the marker genes for both normal and tumorous B cells. **d.** A cell development trajectory for the four B cell subpopulations, with the line representing the lymphoma development trajectory. **e.** The pseudotime of the four B cell subpopulations. **f.** The pseudotime of the four B cell subpopulations. Color represents cell clusters, and the Y-axis is the enrichment score. **g.** The regulatory relationship of the PDL1 gene across the four B cell subpopulations. The red color signifies the regulatory score for each enhancer of the STAT1 coding gene across different B cell subpopulations, while blue indicates gene expression. **h.** The regulatory relationship of the PDL1 gene across the four B cell subpopulations. The red color signifies the regulatory score for each enhancer of the HIF1A coding gene across different B cell subpopulations, while blue denotes gene expression across these subpopulations. **i.**

The regulatory relationship of the BCL2 gene (an anti-apoptosis promoting gene) across the four B cell subpopulations. The red color represents the regulatory score of each enhancer for the BCL2 coding gene across different B cell subpopulations, while the blue color represents gene expression in these subpopulations. **j.** Observed and extrapolated future states (depicted as arrows) following the POU2F2 knockout in the four B cell subpopulations. The color represents the different cell clusters. **k.** Observed and extrapolated future states (depicted as arrows) following the FOXP1 knockout in the four B cell subpopulations. The color represents the different cell clusters.

### ***MarsGT identifies MAIT-like rare cell populations and eGRNs in multi-sample melanoma scRNA-seq and scATAC-seq***

To broaden MarsGT's scope in multi-sample and rare cell population inference, we utilized ten matched scRNA-seq and scATAC-seq samples of peripheral blood mononuclear cells (PBMCs) from melanoma patients at baseline (prior to receiving anti-PD1 therapy) and healthy donors. Of these, two samples were from healthy donors, while the remaining eight were from melanoma patients. MarsGT identified 13 distinct cell clusters from the integrated dataset of these ten samples, which include one CD4+T cell group, three CD8+ T cell groups, two CD14+ monocytes (Mono) cell groups, one B cell group, one Nature killing (NK) cell group, one FCGR3A+ Mono cell group, and three Dendritic (DC) cell group. These clusters were annotated by visualizing the expression levels of curated marker genes in the major cell populations (**Fig. 5a, b**). DEGs for each cell population were calculated and represented in a heatmap (**Supplementary Fig. 15**). Notably, we observed two rare cell populations within the CD8+ T cells, namely, Cluster 9 and Cluster 12. The DEGs across these three CD8+ T cell populations were computed (**Supplementary Fig. 16, Supplementary Data 17**), leading to the identification of top DEGs such as ZBTB16 and SLC4A10 in Clusters 9 and 12. These genes act as markers for Mucosal Associated Invariant T cells (MAIT), recognized as a crucial rare cell population in immune responses. To delve deeper into the cell populations within Clusters 9 and 12, we visualized additional MAIT marker genes (**Fig. 5c**). Given that both MAIT and Natural Killer T (NKT) cells are non-canonical T cells and share similarities in their functions and partial marker genes, we computed the gene signature enrichment scores for MAIT and NKT respectively. The MAIT score was significantly higher than the NKT score (**Fig. 5d, Supplementary Data 18**), leading us to define Cluster 9 as MAIT-like 1 and Cluster 12 as MAIT-like 2.

We constructed the eGRN of the three CD8+ T cell populations and found that common enhancers and genes in the three cell populations constituted the majority proportion (**Fig. 5e, f, Supplementary Data 19**). Meanwhile, each cell population demonstrated unique enhancers and genes, indicating that MAIT-like 1 and MAIT-like 2 represent different MAIT-like subpopulations, each endowed with unique functional attributes. To support this observation, we inferred the pathways enriched in the MAIT-like cell population based on the cell population's active gene expression in the eGRNs (**Fig. 5g**). MAIT-like 1 and MAIT-like 2 shared several pathways, including Regulation of I-

kappaB kinase/NF-kappaB Signaling, which play significant roles in immune responses. Unique to MAIT-like 1 were pathways such as Positive Regulation of Cytokine Production Involved in Immune Response, Interleukin-12-Mediated Signaling Pathway, and Regulation of Type I Interferon Production. The MAPK Cascade pathway was unique to MAIT-like 2, further differentiating these two subpopulations. Divergent regulatory patterns became apparent when we focused on a single regulon, ZBTB16, recognized as a critical transcription factor in MAIT cells. We visualized the expression of the genes it regulates, as well as the average accessibility value of the peaks associated with these regulated genes (**Fig. 5h**). We further mapped the regulatory relationships of ZBTB16 within the two MAIT-like cell populations (**Fig. 5i**). Interestingly, our results highlight minor differences in expression and accessibility, but more substantial variations in regulatory relationships. This supports our hypothesis that regulatory information is pivotal in recognizing rare cell populations.

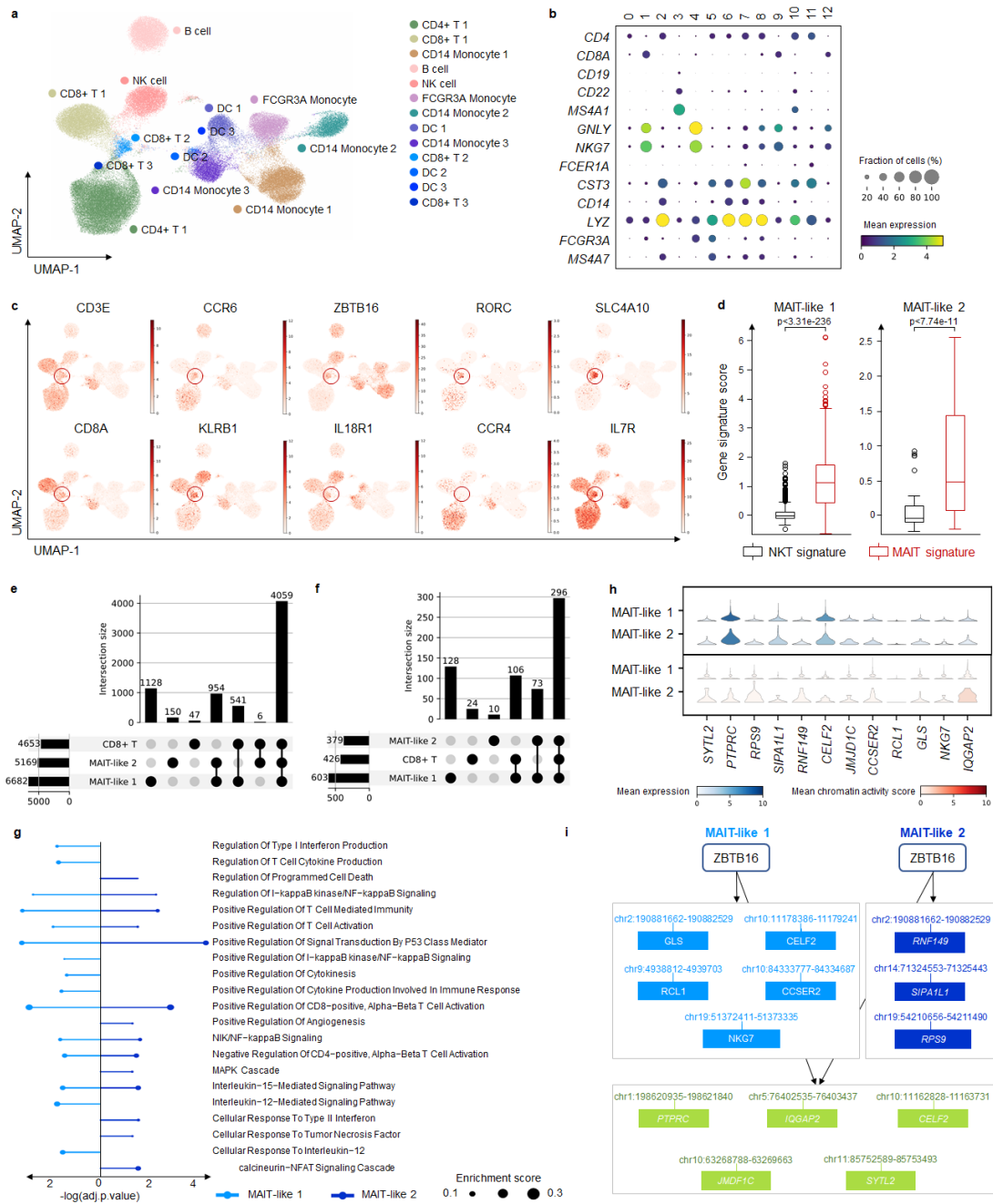


**Fig. 5. MarsGT identifies MAIT-like rare cell populations and eGRNs in multi-sample melanoma scRNA-seq and scATAC-seq.** **a.** UMAP visualizes MarsGT's predicted cell cluster results, annotated based on marker genes. **b.** Dotplot depicts the expression value and proportion of marker genes within the cell clusters predicted by MarsGT. **c.** UMAPs showcases the marker genes of MAIT cells. **d.** showcasing the marker genes of MAIT cells. The p-value is calculated by the Mann-Whitney U test with one-sided. **e.** The upset plot illustrates the peaks present in CD8+ T cell subpopulations. **f.** The upset plot demonstrates the genes found in CD8+ T cell subpopulations. **g.** Pathway enrichment across different MAIT-like cell populations. Colors represent distinct cell populations, while the size of the dots indicates the ratio of enriched genes. **h.** The expression and accessibility of ZBTB16-regulated genes across various MAIT cell populations. **i.** The regulatory relations of ZBTB16 in different MAIT-like cell

populations. Green means the common regulatory relations between MAIT-like 1 and MAIT-like 2. Light blue means the regulatory relations unique in MAIT-like 1. Dark blue means the regulatory relations unique in MAIT-like 2.

### ***MarsGT reveals the mechanism for different survival of PD1-blocking immunotherapy***

The above ten sample datasets we analyzed incorporated immunotherapy data from eight melanoma patients, grouped according to their Interferon-I response capacity (IRC). Four patients exhibited high IRC, as determined by the levels of Interferon-I stimulated proteins measured by mass cytometry, while the remaining four demonstrated low IRC (**Supplementary Fig.17**). The source study inferred that a hyporesponsive IRC effectively predicted extended survival following PD1-blocking immunotherapy, while high responsiveness strongly associated with treatment failure and reduced survival duration. Interestingly, we observed that in both MAIT-like 1 and MAIT-like 2 cells, samples with low IRC represented a majority, accounting for 83.57% and 70.18%, respectively, a figure significantly higher than those with high IRC (**Fig. 6a**). Given the potential significance of MAIT-like 1 cells in understanding the survival mechanisms underpinning PD1-blocking immunotherapy, we decided to investigate this cell population further (MAIT-like 2, with only 69 cells, was excluded due to potential low confidence). We found 176 MAIT-like 1 cells in the high IRC group, compared to 895 cells in the low IRC group (**Fig. 6b**). Additionally, the count of DCs in the low IRC group exceeded those in the high IRC group. We compared the expression of IFN-I stimulated genes (ISGs) between high and low IRC patients.

Contrary to the IRC assignments, ISG expression in low IRC patients was significantly higher than in high IRC patients (**Fig. 6c**). Upon calculating the unique enhancers in the eGRNs of high IRC and low IRC groups, respectively, we found that transcription factors TCF1 and BCL6 were exclusively present in the low IRC group. Previous studies have demonstrated that the TCF1-Bcl6 axis counteracts type I interferon to repress exhaustion and maintain T cell stemness<sup>54</sup>. Then we calculated the effector and exhaustion gene signature scores for MAIT cells in high IRC and low IRC groups, respectively (**Fig. 6d, Supplementary Data 20**). MAIT-like 1 cells in the high IRC group appeared exhausted, while those in the low IRC group appeared effective. This observation may explain the varying IRC across samples and the improved prognosis for low IRC patients following PD1-blocking immunotherapy.

High IRC suppressed MAIT-like 1 cells response by triggering high interleukin-10 (IL-10) production by DC, which subsequently inhibited the secretion of IL-15, IL-18 which are costimulatory cytokines for MAIT-like 1 cell activation (**Fig. 6e**). The effector functions of MAIT-like 1 cells are mediated through the production of IFN-II, GzmB, and Perforin. This observation is supported by the expression levels of the genes coding for these cytokines and their respective receptors (**Fig. 6f, g**). Our attention then turned to the regulatory mechanisms of IFN-II, GzmB, and Perforin in the high and low IRC contexts. In low IRC, IFN-I signaling is relayed by Tyk2-NFKB to regulate



IFNG (the coding gene of IFN-II), and relayed by Jak1-STAT1 to regulate GZMB. IL-15 signaling is relayed by Jak1/Jak3-STAT1 to regulate GZMB, while IL-18 signaling is relayed by JNK-NFKB to regulate IFNG and by JNK-FOS/JUN to regulate GZMB and PRF1 (the coding gene of Perforin). In contrast, high IRC sees only IL-18 signaling relayed by JNK-FOS/JUN to regulate PRF1 (**Fig. 6i**). The complete GRNs of IFNG, GZMB, and PRF1 are depicted in **Supplementary Fig. 18**. Interestingly, we observed a higher number of positive regulatory relations in low IRC compared to high IRC. This suggests a critical role for low IRC in facilitating the elimination of tumor cells. In other words, compared to samples with high IRC, those with low IRC stimulate the expression of cytokine and cytolytic molecule coding genes in CD8+ T cells via various costimulatory factors and pathways. This leads to the enhanced secretion of IFN- $\gamma$ , TNF- $\alpha$ , Granzyme B, and Perforin, which in turn boosts the cytotoxic function of CD8+ T cells, promoting more effective tumor destruction.

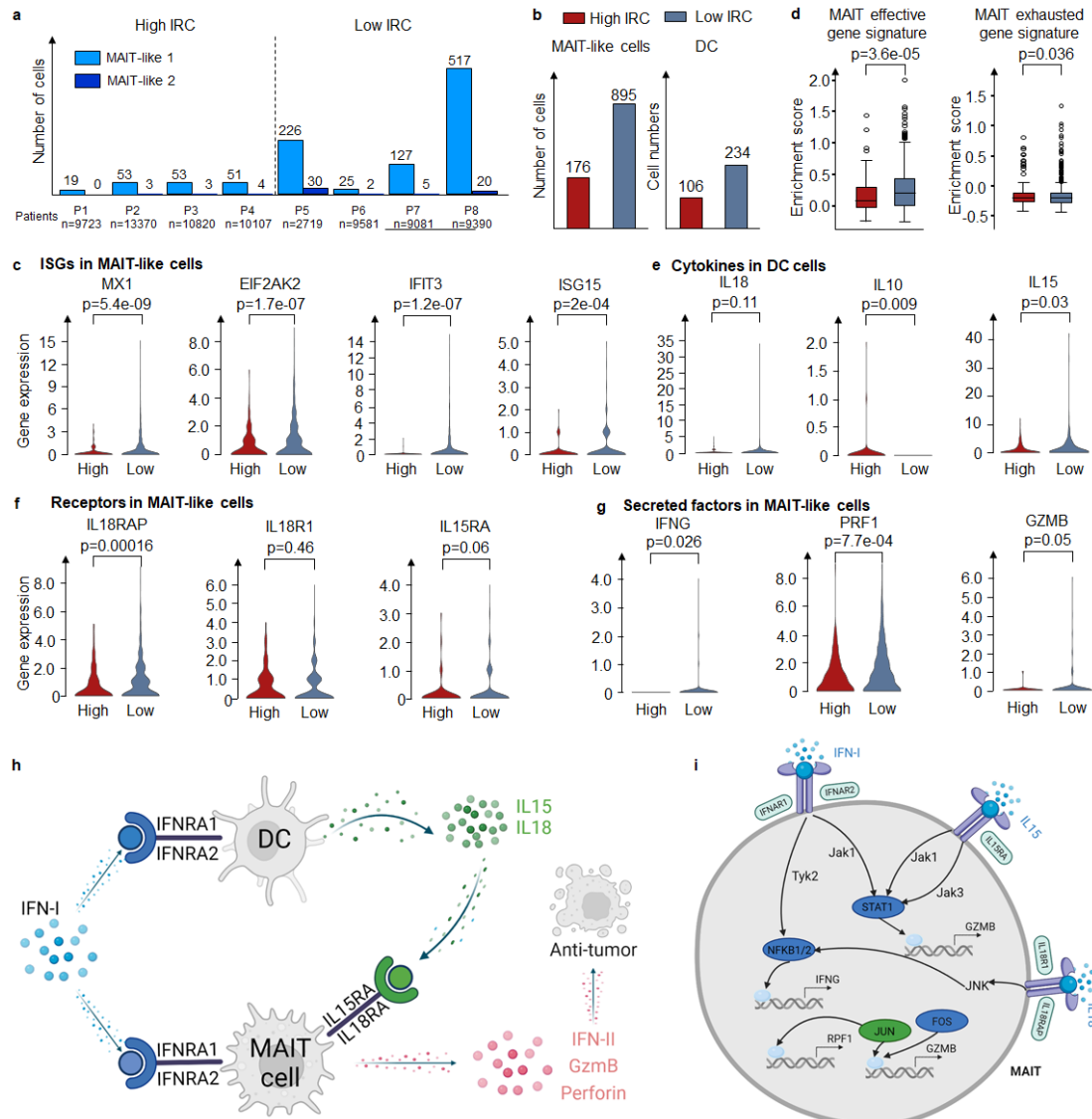


**Fig. 6. MarsGT reveals the good prognosis with high IFN-I response impairs MAIT cell responses by increasing IL10 and inducing IL15 and IL12 from DC. a.** The number of cells

in MAIT-like cell populations in different melanoma patients. **b.** The number of cells in MAIT cells and DC cells in high IRC and low IRC. **c.** Enrichment score of MAIT effective gene signature and exhausted gene signature across varying IRC. **d.** The expression of critical genes (including ISGs, receptor coding genes, and the coding gene of secretion) in different IRC in MAIT cells. **e.** Expression of IFN-I receptor coding genes in MAIT cells across different IRC. **f.** Expression of critical cytokine genes in DC cells across varying IRC. **g.** The expression of secreted factors coding genes in MAIT cells across different IRC. **h.** The mechanism of MAIT-like cells with different IRC samples. **i.** The regulatory mechanism of IFN-II, GzmB, and Perforin in high IRC and low IRC. Green means the common regulatory relations between high IRC and low IRC. Dark blue means the regulatory relations are unique in low IRC. All the p-values are calculated by the Mann-Whitney U test with one-sided.

## Discussion

MarsGT is an end-to-end deep learning model capable of inferring and identifying rare cell populations from scMulti-omics data using a heterogeneous graph transformer. To model and represent the scMulti-omics data, a heterogeneous graph is constructed, comprising nodes of cells, genes, and peaks. This configuration allows for the updating of joint embeddings of cells, genes, and peaks, facilitated by a multi-head attention mechanism. An end-to-end model benefits rare cell identification as it integrates scMulti-omics data with minimal information loss. The graph transformer can enhance the signal-to-noise ratio, addressing the high dropout feature of single-cell technologies, which in turn reduces the false positive rate in rare cell identification. Crucially, MarsGT employs a novel probability-based subgraph-sampling technique during model training, which allows the selective highlighting of cell-gene and cell-peak relationships that are relevant to rare cells. In parallel, the model determines peak-gene relations and rare cell populations from the subgraphs, undergoing iterative updates during the training process. Consequently, MarsGT is well equipped to identify rare cell populations and their corresponding gene regulatory networks within the entire heterogeneous graph.

MarsGT's performance remains consistent across data types (snRNA-ATAC-seq or scRNA-ATAC-seq), health statuses (healthy or diseased), and species (human or mouse). In the mouse retina case, MarsGT identified not only six major cell populations but also a rare sub-cell population of Müller glia cells, a discovery unachievable by alternative computational tools and unreported in the original study. In the human small lymphocytic lymphoma case, MarsGT pinpointed a rare B cell lymphoma population, with unique transcription factors and binding enhancer changes indicating potential regulatory mechanisms, functional differences, and a possible precursor state for B cell lymphoma. This finding could lead to early detection or prevention strategies for B cell lymphoma progression. In the melanoma case, MarsGT identified two CD8+ Mucosal-associated invariant T (MAIT)-like rare subpopulations and revealed that high IFN-I response hinders these MAIT-like cell responses by upregulating IL10 and inducing IL15 and IL12 from DC in patients who responded to immune checkpoint blockade. These examples underscore the prowess of MarsGT in uncovering new

biological insights, as well as generating new biomarkers for guiding immunotherapy.

While MarsGT shows impressive performance in identifying rare cells and uncovering novel biological insights, there is room for improvement. Statistical significance is crucial for rare cell identification to ensure that detected rare cell populations genuinely exist, rather than being random false positives. In this study, we utilized scPOWER to maintain high-confidence rare cell populations. It is necessary to develop a new method for significance testing. More complex scenarios, such as senescent cells that exhibit high heterogeneity even within the same cell type, also need to be considered. For multi-sample datasets, batch correction is necessary prior to the MarsGT application. Thus, developing an algorithm that can perform batch correction during training could enhance the utility of MarsGT. Moreover, the model's dependency on GPU computations might challenge reproducibility. While our benchmark tests demonstrate negligible variance across multiple runs, the small number of rare cell populations identified suggests that the focus should be on significant findings for analysis. In conclusion, MarsGT represents a novel tool for the identification of rare cell populations and the elucidation of microenvironmental and immunotherapeutic mechanisms. It sets a promising trajectory for precision medicine by enabling the discovery of disease-associated rare cell populations and uncovering intrinsic regulatory mechanisms that could inform immunotherapy strategies.

## Online Methods

### Data preprocessing

MarsGT initiates by inputting the raw count matrices derived from matched scRNA-seq  $X^R = \{x_{ik}^R | i = 1, 2, \dots, M_1; k = 1, 2, \dots, N\}$  and scATAC-seq  $X^A = \{x_{jk}^A | j = 1, 2, \dots, M_2; k = 1, 2, \dots, N\}$ . For the scRNA-seq data matrix, we organize it such that rows represent genes, whereas cells constitute the columns. Conversely, the scATAC-seq data matrix is structured with regulatory regions (peaks) as rows and cells as columns. Any row or column in each data matrix containing less than 0.1% non-zero values is excluded from further analysis. Quality control measures for the data are conducted utilizing Seurat v3<sup>55</sup>, encompassing criteria like total read counts and mitochondrial gene ratios.

We then construct the regulatory score matrix  $X^{RA} = \{x_{ij}^{RA} | i = 1, 2, \dots, M_1; j = 1, 2, \dots, M_2\}$  based on MAESTRO<sup>56</sup>. In this matrix,  $x_{ij}^{RA}$  signifies the regulatory potential of peak  $j$  relative to gene  $i$ . This potential is determined in accordance with the genomic distance between peak  $j$  and gene  $i$ .

$$x_{ij}^{RA} = \begin{cases} 0, & d_{ij} > 150\text{kb} \text{ or peak } j \text{ located in any nearby genes} \\ 2^{-\frac{d_{ij}}{d_0}}, & \text{peak } j \text{ located at the exon regions of the gene } i \\ \frac{2^{-\frac{d_{ij}}{d_0}}}{\text{Length}(\text{exon})}, & \text{peak } j \text{ located at the exon regions of the gene } i \\ 2^{-\frac{d_{ij}}{d_0}}, & \text{else} \end{cases} \quad (1)$$

The distance between the center of peak  $j$  and the transcription start site of gene  $i$  is denoted as  $d_{ij}$ . The half-decay of the distance,  $d_0$ , is set to be 10kb. As indicated by

formula (1), the regulatory potential score  $x_{ij}^{RA}$  of peak  $j$  relative to gene  $i$  is typically calculated by  $2^{-\frac{d_{ij}}{d_0}}$ ; For peaks with  $d_{ij} > 150kb$ , we conveniently assign the regulatory potential score of 0, considering that it will be less than 0.0005. For peaks located within the exon region where  $d_{ij}$  is 0,  $x_{ij}^{RA}$  is computed as  $\frac{1}{Length(exon)}$  as per the formula.

### Multiple datasets integration

In our specific case analysis, we handled matched scRNA-seq and scATAC-seq across multiple samples. For batch effect correction in multiple scRNA-seq datasets, we employed Harmony<sup>57</sup>, resulting in an integrated matrix. For multiple scATAC-seq datasets, we adopted a binning approach with a length of 5,000 base pairs to amalgamate different samples. The counts of peaks falling within the same bin were aggregated. Subsequently, multiple scATAC-seq datasets were integrated into a single matrix, where rows represented bins and columns denoted cells.

### MarsGT model's construction

**Heterogeneous graph construction.** To integrate matrices  $X^R$  and  $X^A$ , we construct a gene-cell-peak heterogeneous graph  $G$ , consisting of three node types and four edge types. We define the heterogeneous graph as  $G = (V, E, F)$  with node set  $V = V^C \cup V^E \cup V^G$ , where  $V^C = \{v_k^C | k = 1, 2, \dots, N\}$  denotes all cells,  $V^E = \{v_j^E | j = 1, 2, \dots, M_2\}$  denotes all peaks,  $V^G = \{v_i^G | i = 1, 2, \dots, M_1\}$  denotes all genes. The edge set  $E$  is constituted as  $\{(v_i^G, v_k^C), (v_k^C, v_i^G), (v_j^E, v_k^C), (v_k^C, v_j^E) | i = 1, 2, \dots, M_1, j = 1, 2, \dots, M_2, k = 1, 2, \dots, N\}$ , with edge weight  $w$  defined as follows. To eliminate information redundancy between node initial embeddings and the edge weights, we utilize unweighted edges when constructing the heterogeneous graph. For  $X_{ik}^R > 0$ ,  $w(v_i^G, v_k^C) = w(v_k^C, v_i^G) = 1$ , otherwise,  $w(v_i^G, v_k^C) = w(v_k^C, v_i^G) = 0$ . For  $X_{jk}^A > 0$ ,  $w(v_j^E, v_k^C) = w(v_k^C, v_j^E) = 1$ , otherwise,  $w(v_j^E, v_k^C) = w(v_k^C, v_j^E) = 0$ . Lastly, we establish the initial feature vectors  $F$  for nodes in  $G$  as follows:

$$\begin{aligned} F_k^C &= X_{\cdot, k}^R, \quad k = 1, 2, \dots, N; \\ F_j^E &= (X_{j, \cdot}^A)^T, \quad j = 1, 2, \dots, M_2; \\ F_i^G &= (X_{i, \cdot}^R)^T, \quad i = 1, 2, \dots, M_1; \end{aligned}$$

where  $X_{i, \cdot}$  and  $X_{\cdot, k}$  represent the  $i_{th}$  row vector and the  $k_{th}$  column vector of  $X$ , respectively.

**Sub-sampling of a heterogeneous graph.** To enhance the efficiency of MarsGT when dealing with an expansive heterogeneous graph, it is necessary to select subgraphs prior to model training. It is reasonable to suggest that a ubiquitously highly expressed gene or highly accessible enhancer may not play a significant role in identifying rare cells. Consequently, for cell  $k_0$ , we selected a number (with 20 as

default) of highly expressed genes (for  $x_{ik_0}^G > a$ )  $v_{ik_0}^G$  within the cell according to a defined probability which is as follows:

$$\text{prob}(v_{ik_0}^G) = \frac{x_{ik_0}^R}{\sum_k x_{ik}^R} \quad (2)$$

where  $a$  is a threshold set to the first quartile of the expression value. As  $X^A$  trends towards binarization, we select a predetermined number (with 20 as default) of highly accessible peaks  $v_{jk_0}^E$  within the cell according to a probability that is defined as follows:

$$\text{prob}(v_{jk_0}^E) = \frac{x_{jk_0}^A}{\sum_k x_{jk}^A} \quad (3)$$

Each subgraph incorporates 30 cells randomly along with their selected neighbor nodes. MarsGT is trained using multiple mini-batches, each represented by a subgraph.

**MarsGT embedding update.** Let  $H^l$  represent the embedding of the  $l^{\text{th}}$  layer ( $l=1, 2, \dots, L$ ). The embedding of  $v_i^G$ ,  $v_j^E$ ,  $v_k^C$  on the  $l^{\text{th}}$  the layer is denoted as  $H^l[v_i^G]$ ,  $H^l[v_j^E]$ , and  $H^l[v_k^C]$ , respectively. The initial embeddings are denoted as  $H^0[v_i^G] = F_i^G$ ,  $H^0[v_j^E] = F_j^E$ , and  $H^0[v_k^C] = F_k^C$ . To align the features of different types of nodes into the same dimension, we apply a linear projection function  $W$  to map initial node embeddings into a lower dimension, which we set at 256:

$$H^1[v_i^G] = W_G(H^0[v_i^G]) \quad (4)$$

$$H^1[v_j^E] = W_E(H^0[v_j^E]) \quad (5)$$

$$H^1[v_k^C] = W_C(H^0[v_k^C]) \quad (6)$$

Subsequently, we apply a multi-head mechanism to divide  $H^1[v]$  evenly into  $h$  heads. Within the  $l^{\text{th}}$  layer for the  $h^{\text{th}}$  head, three linear projection functions, query ( $Q$ ), key ( $K$ ), and value ( $V$ ). For each node  $v$  within the graph, the embeddings following the linear transformation are denoted as follows:

$$Q^h(v) = Q^h(H^1[v]) \quad (7)$$

$$K^h(v) = K^h(H^1[v]) \quad (8)$$

$$V^h(v) = V^h(H^1[v]) \quad (9)$$

To calculate the mutual attention between node  $v$  and its neighbor  $N(v)$  within the  $h^{\text{th}}$ , we introduce the attention operator. This operator estimates the importance of each neighboring node  $v^{ne}$  in  $N(v)$  relative to  $v$  using  $K^h(v_n)W_{t(v_n,v)}^{ATT}Q^h(v)^T$ ,

where  $W_{t(v_n,v)}^{ATT}$  is a transformation matrix designed to capture edge features, while  $t(\cdot)$  denotes the edge type.  $(\cdot)^T$  signifies the transposal function. The attention coefficient within the head  $h_0$  is then calculated as follows:

$$\text{att}(v^{ne}, v, h_0) = \underset{v^{ne} \in N(v)}{\text{Softmax}}(K^{h_0}(v^{ne})W_{t(v^{ne},v)}^{ATT}Q^{h_0}(v)^T) \quad (10)$$

The concatenation of attention heads yields the attention coefficients, represented as follows:

$$\text{att}(v^{ne}, v) = \parallel_h(\text{att}(v^{ne}, v, h)) \quad (11)$$

The message from  $v^{ne}$  that can be relayed to  $v$  within head  $h$  is given by  $V^h(v^{ne})W_{t(v^{ne}, v)}^{MSG}$ .  $W_{t(v^{ne}, v)}^{MSG}$  is also a transformation matrix. Then, the results from different message heads should subsequently be concatenated:

$$\text{mes}(v^{ne}, v) = \parallel_h V^h(v^{ne})W_{t(v^{ne}, v)}^{MSG} \quad (11)$$

To update the embedding of node  $v$ , the final step within the  $l^{th}$  layer to update the embedding of the node in the  $H^{l-1}[v]$  and  $H^l[v]$  into the node's embedding.

$$H^l[v] = \underset{\forall v^{ne} \in N(v)}{\text{Aggregate}} \text{att}(v^{ne}, v) \text{mes}(v^{ne}, v) \quad (12)$$

$$H^l[v] = \alpha \text{ReLU}(H^l[v]) + (1 - \alpha)H^{l-1}[v] \quad (13)$$

where  $\alpha$  represents a trainable parameter, while ReLU functions as the activation function. The final embedding of  $v$  is obtained by layer-wise stacking of information.

**MarsGT subgraph training.** For the sake of generality, we continue using the aforementioned notation for subgraphs. Following the calculation of embeddings, all nodes (genes, cells, and peaks) acquire new embeddings, denoted as  $\{H^l[v] | v \in V^C \cup V^E \cup V^G\}$ . The update embeddings of cells  $H^l[v] | v \in V^C$  is denoted as  $P$  after Softmax operation. Each row of  $P$  represents a cell, each column of  $P$  represents a reduced dimension set manually, and each element signifies the probability that a cell belongs to a specific cell cluster. We establish an initial number of cell clusters that align with the number of cell embeddings. A cell is assigned to the cell cluster where the corresponding dimension yields the highest value relative to all other dimensions. Thus, MarsGT does not require pre-specification of the number of cell clusters. Similarly, we construct the initial embedding of links between genes and peaks for each cell cluster by concatenating gene and peak embeddings, denoted as  $Q$ . The row of  $Q$  represents a peak-gene link, and the column of  $Q$  represents the cell cluster. By applying a linear layer and a ReLU layer, the dimension of  $Q$  is reduced to match the number of initial cell clusters. The output is the probability that a peak-gene link belongs to each cell cluster which is denoted as  $\hat{O}$ . The base peak-gene relations are determined based on  $X^{RA}$  and adjusted according to the corresponding gene expressions and chromatin accessibility of all cells in a cell cluster, denoted as  $O$ .

In our model training, we devise a multi-faceted loss function, which consists of four critical components.

- (i) We employ a Kullback-Leibler (KL) divergence score to assess the disparity between the original input expression/accessibility matrices and the reconstructed matrices. These reconstructed matrices are derived from the dot product of the updated embeddings of genes/peaks and cells. As the KL

divergence diminishes, less information is lost during heterogeneous graph transformer (HGT) learning.

- (ii) Cosine similarity serves to gauge the similarity among cells within the same cell cluster, which is derived from the cell embeddings. A higher similarity score indicates superior clustering efficacy.
- (iii) We utilize another KL divergence score to evaluate discrepancies between predicted and baseline peak-gene links within each cell cluster. The baseline peak-gene associations are determined based on proximity to the nearest genes. Further, we calculate an activity score founded on regulatory potential, employing MAESTRO, and adjust this score according to the corresponding gene expressions and chromatin accessibility across all cells within a cell cluster.
- (iv) We calculate an entropy score to contrast the differences between the base and predicted cell clustering outcomes. The base cell clusters are ascertained by implementing the Louvain clustering method on the initial cell embeddings. It's imperative to ensure that the quantity of peak-gene links in the predictions does not exceed known links.

This entropy score functions as a regularizing term in our loss function, which is defined as follows:

$$Loss = KL_{cluster} + Cos_{loss} + KL(\hat{O}, O) + Reg_{loss} \quad (14)$$

where  $KL_{cluster} = KL(H^l[V^G] * H^l[V^C]^T, X^R)$ .

The Cosine similarity in cluster  $C_0$  is defined as:

$$Cos_{loss} = \sum_{\forall k_a, k_b \in C_0} Cosine(H^l[V^{k_a}], H^l[V^{k_b}]) \quad (15)$$

The regular term is defined as:

$$Reg_{loss} = Smoothing_{cross}(P, L, \varepsilon) \quad (16)$$

where  $L = \{l_k | l_k \in \{1, 2, \dots, T\}\}$  is the cell cluster results by Louvain with scRNA-seq,  $T$  is the number of cell clusters by Louvain,  $\varepsilon$  is a smoothing factor.

$$Smoothing_{cross}(P, L, \varepsilon) = \begin{cases} (\varepsilon - 1) \sum_{k=1}^N l_k \log p_k & \text{if } (l_k = p_k) \\ -\varepsilon \sum_{k=1}^N l_k \log p_k & \text{if } (l_k \neq p_k) \end{cases} \quad (17)$$

where  $p_k$  represents the predicted cell clustering result for cell  $k$ . Our algorithm concurrently updates the cell clustering outcomes and the peak-gene links within each set of cell cluster prediction results. The model is designed to iterate until it reaches a state of convergence, at which point we obtain the cell clusters and all peak-gene links specific to each cluster. Following this, the peak-gene links within each cell cluster are obtained.

**MarsGT predicts cell clusters and eGRN in the whole graph.** Upon completing the two phases of training, a robustly trained model is generated. To ensure that every cell is mapped to its corresponding predicted cluster, and every gene and peak is associated with cell cluster-specific peak-gene regulatory information, we apply the trained model to the entire graph. By covering all cells through the chosen union of subgraphs, the trained model, when applied to the entire graph, can also have a good performance. The cell cluster predictions encompass all cells. Regarding cell cluster-

specific peak-gene link, we use the final predicted cell cluster results to calculate all genes and peaks, eschewing the use of a subgraph. In order to quantify the specific degree of each peak-gene link, we determine the peak-gene score based on gene expression, peak accessibility, and the regulatory potential of peaks to genes. The peak-gene link score (PGS) is defined as:

$$PGS(i, j, CT) = \{x_{i \times j, CT} = \frac{\sum_k^{|CT|} x_{ik}^R \times x_{ij}^{RA} \times x_{jk}^A}{|CT|} \mid i = 1, 2, \dots, M_1, j = 1, 2, \dots, M_2, k = 1, 2, \dots, N\} \quad (18)$$

where  $|CT|$  is the cell number in cell cluster  $CT$ . Then the cell cluster corresponding peak-gene links are inferred. To infer eGRN, we need to introduce the TF information. We retrieved the genome browser track file from JASPAR, which stores all known TF binding sites of each TF. A p-value score was provided in JASPAR. We removed TF binding sites with p-value scores more than 0.05. And then, if a TF binding site overlaps with any peak regions in the predicted peak-gene link, it will be kept, otherwise, removed. Finally, the TF-peak relations will be obtained, and the eGRNs in each cell cluster also are inferred.

## Benchmark of rare cell population identification

### *Simulated single-cell multi-omics data*

We evaluated the performance of rare cell identification based on the algorithm's capability to distinguish between two known rare populations. We assessed the algorithm's efficacy using 400 simulated datasets with eight different designs from two different data types. The first data type consisted of cell line data (549 cells) characterized by low intra-class heterogeneity, available at <https://trace.ncbi.nlm.nih.gov/Traces/sra/sra.cgi?study=SRP136421>. This data contained five cell line types: PDX1, PDX2, HeLa.S3, K562, and HCT116. The second type was the immune population dataset (17,243 cells) with high intra-class heterogeneity, obtainable from <https://www.ncbi.nlm.nih.gov/geo/query/acc.cgi?acc=GSE194122>. In the cell line dataset, we selected PDX1 (176 cells) and PDX2 (167 cells) as the common cell populations, while HeLa.S3 (42 cells) and K562 (74 cells) were chosen as the rare population in the simulated data. Two types of simulated datasets were created based on the cell line data (**Supplementary Table S1**). Each dataset consisted of 50 datasets, each containing 300 cells that were randomly subsampled from each cell type. Similarly, for PBMC cells, we utilized NK, CD4+T naïve, CD8+T (common), Erythroblast, Plasma, HSC, and ID2-hi myeloid prog cells (rare) to establish six types of simulated datasets (**Supplementary Table S1**). There were 50 datasets of 500 cells generated by randomly subsampling from each cell type.

To assess the proportion of rare cells detected by different software, datasets were created to include from 970 to 995 common cells and 30 to 5 rare cells. For instance, the smallest common dataset was comprised of 970 common cells and 30 rare cells (3%), while the largest included 995 common cells and 5 rare cells (0.5%). Six datasets of 1000 cells, with differing rare cell proportions, were generated by random subsampling from each cell type. The first five datasets tested rare cell population



identification, while the sixth assessed the false-positive rate of each algorithm. All algorithms were applied to these datasets with default or suggested settings. The results were visualized using UMAP for Scanpy and colored by predicted results.

### ***Simulated datasets benchmarking quantification***

To optimize the default parameters of MarsGT, we conducted a grid-search test on seven simulated datasets. The parameters considered in this optimization included weighted decay (0, 0.1, 0.3), learning rate (0.001, 0.0005), and label smoothing (0, 0.1, 0.3), which are important parameters to prevent overfitting and ensure convergence speed. This resulted in a total of 18 unique parameter combinations. We randomly selected one dataset from each type of simulation as a training set. The most effective parameter combination was weighted decay = 0.1, learning rate = 0.001, and label smoothing = 0.3. This set was subsequently adopted as the default parameter combination. The remaining simulation datasets were processed using these default parameters.

### ***Real datasets benchmarking quantification***

To assess the generalizability of our model, we applied the same parameter combinations that we used with the simulated datasets to three benchmark (PBMC-bench-1, 2, 3) real datasets. We subsequently employed the default parameters for an independent test dataset (PBMC-test).

### ***The ability of rare cell identification***

Typically, a cell type is classified as rare if it constitutes less than 3% of the total cell count. However, truly rare cell types often represent much less than this threshold. To evaluate the capacity of various tools to identify these rare cells, we designated cell types representing 0.5%, 1%, 2%, and 3% of the total cell count as rare in the independent test dataset. We then calculated the F1 score, precision, and recall score for each category.

### ***Reproducibility test***

To evaluate the stability and reproducibility of MarsGT, we executed the algorithm 20 times on the independent test dataset, utilizing the default parameters. We then computed the variance of several key metrics, including the F1 score, precision, recall score, Normalized Mutual Information (NMI), purity, and entropy.

### ***Baseline tools parameter set***

To evaluate the performance of MarsGT relative to other tools for identifying rare cells, we conducted a comparative analysis between MarsGT and other established methods.

- (i) FIRE<sup>4</sup> (v 1.0.1, <https://github.com/princethewinner/FIRE>, data pre-processing, and feature extraction uses the function “ranger\_preprocess”).
- (ii) GapClust<sup>13</sup> (v 0.1.0, <https://github.com/fabotao/GapClust>, genes that were expressed in less than three cells were excluded, and cells expressing <200 genes

were also excluded, the normalization procedure was accomplished using the scran (R package).

- (iii) CellSIUS<sup>26</sup> (v 1.0.0, <https://github.com/Novartis/CellSIUS>, cells were filtered based on the total number of detected genes, total UMI counts, and the percentage of total UMI counts attributed to mitochondrial genes, genes have to present with at least 3 UMIs in at least one cell. After this initial QC, the remaining outlier cells were identified and removed using the plotPCA function from the scatter (R package with detect\_outliers set to TRUE). Data were normalized using scran (R package), including a first clustering step as implemented in the “quickCluster” function).
- (iv) RaceID<sup>2</sup> (v 0.2.3, [https://github.com/dgrun/RaceID3\\_StemID2\\_package](https://github.com/dgrun/RaceID3_StemID2_package)).
- (v) GiniClust<sup>15</sup> (v 3.0, <https://github.com/rdong08/GiniClust3>, the “neighbors” parameter of the function “clusterGini” is set to 10 (the recommended value is from 5 to 15), other parameters at the default values).
- (vi) SCMER<sup>1</sup> (v 0.1.0a3, <https://github.com/KChen-lab/SCMER>, data pre-processing is carried out using Scanpy (Python package)).

For each benchmarking tools, grid tests were also applied to a combination of parameters (**Supplementary Data 5**).

### Evaluation index

To assess the precision of various rare cell identification algorithms, we employed metrics quantifying the purity of the clustering output. We evaluated two categories of algorithms: the first encompassing clustering methods capable of differentiating all cell populations, such as SCMER<sup>1</sup>, GiniClust<sup>15</sup>, and RaceID<sup>2</sup>, and the second consisting of classification methods that can distinguish only between rare cell and major cell populations. For evaluating clustering methods, we utilized purity, entropy, and Normalized Mutual Information (NMI). For assessing classification methods, we applied recall, precision, and F1-score metrics.

**Purity** is based on the frequency of the most abundant class in the predicted clusters. Let  $S = \{s_1, s_2, \dots, s_S\}$  be the set of predicted clusters, and  $T = \{t_1, t_2, \dots, t_T\}$  be the set of true labels. The purity index is defined as:

$$purity(S, T) = \frac{\sum_s \max_t |s_s \cap t_t|}{N} \quad (19)$$

where  $s_s$  ( $t = 1, \dots, S$ ) is the set of cells in the predicted clusters.  $t_t$  ( $t = 1, \dots, T$ ) is the set of cells in the true labels.  $N$  is the number of cells. The value of purity ranges from 0 to 1, where 1 provides the best clustering effect.

**Entropy** uses Shannon entropy to evaluate cluster accuracy by measuring the expected amount of information from the clusters. Let  $S = \{s_1, s_2, \dots, s_S\}$  be the set of predicted clusters, and  $T = \{t_1, t_2, \dots, t_T\}$  be the set of true labels. The entropy of each predicted cluster  $s$  is defined as:

$$H(s_s) = - \sum_s \frac{|s_{st}|}{|s_s|} \log \frac{|s_{st}|}{|s_s|} \quad (20)$$

$$s_{st} = s_s \cap t_t \quad (21)$$

Then, the entropy for all clusters is defined as:

$$entropy(S, T) = \sum_s \frac{|s_s|}{N} H(s_s) \quad (22)$$

Lower entropy means higher clustering accuracy.

**NMI** measures the normalized dependency of the true labels on the predicted cluster. Mutual information is defined as:

$$I(S, T) = \sum_s \sum_t \frac{|s_{st}|}{N} \log \frac{N|s_{st}|}{|s_s||t_t|} \quad (23)$$

To compare mutual information across different clusters,  $I(S, T)$  is normalized to the  $[0, 1]$ , which is bounded by  $\min [H(S), H(T)]$ , where

$$H(S) = - \sum_s \frac{|s_s|}{N} \log \frac{|s_s|}{N} \quad (24)$$

$$H(T) = - \sum_t \frac{|t_t|}{N} \log \frac{|t_t|}{N} \quad (25)$$

Then, NMI is defined as:

$$NMI(P, T) = \frac{I(S, T)}{\min[H(S), H(T)]} \quad (26)$$

Higher NMI means higher clustering accuracy.

**Precision** represents the ability of the model to correctly predict rare cells among all rare cell predictions.

$$Precision = \frac{TP}{TP + FP} \quad (27)$$

**Recall** represents the model's ability to correctly predict rare cells from actual rare cells.

$$Recall = \frac{TP}{TP + FN} \quad (28)$$

**F1-score** can be interpreted as a weighted average of precision and recall. F1-score ranges from 0, poor classification, to 1, perfect classification:

$$F1 \text{ score} = \frac{TP}{TP + 0.5 * (TP + FN)} \quad (29)$$

$TP$  means the number of cells predicted to be rare in real rare cells.  $FP$  means the number of cells predicted to be rare in real common cells.  $FN$  means the number of cells predicted to be common cells in real rare cells

### Data availability

All data used for benchmarking and case studies are collected from the public domain and can be retrieved using links or accession numbers provided in **Supplementary Data 1**.

## Code availability

MarsGT is a user-friendly, efficient package developed in Python, leveraging the capabilities of PyTorch. The source code and vignettes of **MarsGT** are freely available at <https://github.com/mtduan/marsgt>. The source code is also available on Zenodo at <https://zenodo.org/record/8160180>.

## Acknowledgments

This work was supported by awards R01DK138504, P01CA278732, and U54-AG075931 from the National Institutes of Health (NIH). This work was also supported by the Pelotonia Institute of Immuno-Oncology (PIIO). The content is solely the responsibility of the authors and does not necessarily represent the official views of the NIH and PIIO.

## Contributions

Q.M. and B.L. conceived the basic idea. X.W. designed the algorithm, conducted the case study, and wrote the manuscript. M.D. carried out benchmark experiments and wrapped the code. A.M. and M.D. participated in the case analysis. J.L. collected the data and pre-processed the data. A.M. led the figure design. Z.L. provided immunological knowledge. D.X. provided deep learning knowledge. All authors participated in the interpretation and writing of the manuscript.

## Ethics declarations

Competing interests

*The authors declare no competing interests.*

## References

- 1 Liang, S. H. *et al.* Single-cell manifold-preserving feature selection for detecting rare cell populations. *Nat Comput Sci* **1**, 374-384, doi:10.1038/s43588-021-00070-7 (2021).
- 2 Grun, D. Revealing dynamics of gene expression variability in cell state space. *Nature Methods* **17**, 45-+, doi:10.1038/s41592-019-0632-3 (2020).
- 3 Wen, L. & Tang, F. Computational biology: How to catch rare cell types. *Nature* **525**, 197-198, doi:10.1038/nature15204 (2015).
- 4 Jindal, A., Gupta, P., Jayadeva & Sengupta, D. Discovery of rare cells from voluminous single cell expression data. *Nat Commun* **9**, doi:ARTN 4719 10.1038/s41467-018-07234-6 (2018).
- 5 Arvaniti, E. & Claassen, M. Sensitive detection of rare disease-associated cell subsets via representation learning. *Nat Commun* **8**, 14825, doi:10.1038/ncomms14825 (2017).
- 6 Belarif, L., Vanhove, B. & Poirier, N. Full antagonist of the IL-7 receptor suppresses chronic inflammation in non-human primate models by controlling antigen-specific memory T cells. *Cell Stress* **2**, 362-364, doi:10.15698/cst2018.12.168 (2018).

- 7 Hu, X. *et al.* Application of user-guided automated cytometric data analysis to large-scale immunoprofiling of invariant natural killer T cells. *Proc Natl Acad Sci U S A* **110**, 19030-19035, doi:10.1073/pnas.1318322110 (2013).
- 8 Hong, Y. *et al.* The impact of donor characteristics on the invariant natural killer T cells of granulocyte-colony-stimulating factor-mobilized marrow grafts and peripheral blood grafts. *Transpl Immunol* **48**, 55-59, doi:10.1016/j.trim.2018.02.012 (2018).
- 9 Martinez-Lopez, J. *et al.* Monitoring of the Minimum Residual Disease and Depth of Response in Multiple Myeloma. *Haematologica* **104**, 150-150 (2019).
- 10 Pruess, M. *et al.* A High Sensitivity, Tumor-Informed Liquid Biopsy Platform, Designed to Detect Minimum Residual Disease at Part Per Million Resolution. *J Immunother Cancer* **10**, A21-A21, doi:10.1136/jitc-2022-ITOC9.38 (2022).
- 11 Kotliar, D. *et al.* Identifying gene expression programs of cell-type identity and cellular activity with single-cell RNA-Seq. *Elife* **8**, doi:10.7554/eLife.43803 (2019).
- 12 Janssens, J. *et al.* Decoding gene regulation in the fly brain. *Nature* **601**, 630+, doi:10.1038/s41586-021-04262-z (2022).
- 13 Fa, B. T. *et al.* GapClust is a light-weight approach distinguishing rare cells from voluminous single cell expression profiles. *Nat Commun* **12**, doi:ARTN 4197 10.1038/s41467-021-24489-8 (2021).
- 14 Schwartz, G. W. *et al.* TooManyCells identifies and visualizes relationships of single-cell clades. *Nature Methods* **17**, 405+, doi:10.1038/s41592-020-0748-5 (2020).
- 15 Jiang, L., Chen, H. D., Pinello, L. & Yuan, G. C. GiniClust: detecting rare cell types from single-cell gene expression data with Gini index. *Genome Biology* **17**, doi:ARTN 144 10.1186/s13059-016-1010-4 (2016).
- 16 Ma, A. *et al.* Single-cell biological network inference using a heterogeneous graph transformer. *Nat Commun* **14**, 964, doi:10.1038/s41467-023-36559-0 (2023).
- 17 Yi, H. C., You, Z. H., Huang, D. S. & Kwoh, C. K. Graph representation learning in bioinformatics: trends, methods and applications. *Brief Bioinform* **23**, doi:10.1093/bib/bbab340 (2022).
- 18 Yun, S. *et al.* Graph Transformer Networks: Learning meta-path graphs to improve GNNs. *Neural Netw* **153**, 104-119, doi:10.1016/j.neunet.2022.05.026 (2022).
- 19 Zheng, Y. *et al.* A Graph-Transformer for Whole Slide Image Classification. *IEEE Trans Med Imaging* **41**, 3003-3015, doi:10.1109/TMI.2022.3176598 (2022).
- 20 Chu, T., Nguyen, T. T., Hai, B. D., Nguyen, Q. H. & Nguyen, T. Graph Transformer for Drug Response Prediction. *IEEE/ACM Trans Comput Biol Bioinform* **20**, 1065-1072, doi:10.1109/TCBB.2022.3206888 (2023).
- 21 Vaswani, A. *et al.* Attention Is All You Need. *Advances in Neural Information Processing Systems 30 (Nips 2017)* **30** (2017).

- 22 Hu, Z., Dong, Y., Wang, K. & Sun, Y. in *Proceedings of The Web Conference 2020* 2704-2710 (2020).
- 23 Mei, X., Cai, X., Yang, L. & Wang, N. Relation-aware Heterogeneous Graph Transformer based drug repurposing. *Expert Systems with Applications* **190**, doi:10.1016/j.eswa.2021.116165 (2022).
- 24 Gu, H. *et al.* scGNN 2.0: a graph neural network tool for imputation and clustering of single-cell RNA-Seq data. *Bioinformatics* **38**, 5322-5325, doi:10.1093/bioinformatics/btac684 (2022).
- 25 Wang, J. *et al.* scGNN is a novel graph neural network framework for single-cell RNA-Seq analyses. *Nat Commun* **12**, 1882, doi:10.1038/s41467-021-22197-x (2021).
- 26 Wegmann, R. *et al.* CellSIUS provides sensitive and specific detection of rare cell populations from complex single-cell RNA-seq data. *Genome Biology* **20**, doi:ARTN 142 10.1186/s13059-019-1739-7 (2019).
- 27 SenNet, C. NIH SenNet Consortium to map senescent cells throughout the human lifespan to understand physiological health. *Nat Aging* **2**, 1090-1100, doi:10.1038/s43587-022-00326-5 (2022).
- 28 Schmid, K. T. *et al.* scPower accelerates and optimizes the design of multi-sample single cell transcriptomic studies. *Nat Commun* **12**, 6625, doi:10.1038/s41467-021-26779-7 (2021).
- 29 Sun, W., Li, Y.-N., Ye, J.-F., Guan, Y.-Q. & Li, S.-J. MEG3 is involved in the development of glaucoma through promoting the autophagy of retinal ganglion cells. *European Review for Medical & Pharmacological Sciences* **22** (2018).
- 30 Bai, Y., Ma, J.-X. & Le, Y.-Z. The Role of Retinal Müller Cell-Produced VEGF in Ischemia Induced Vascular Leakage. *Investigative Ophthalmology & Visual Science* **50**, 5899-5899 (2009).
- 31 Yan, W. *et al.* Mouse Retinal Cell Atlas: Molecular Identification of over Sixty Amacrine Cell Types. *J Neurosci* **40**, 5177-5195, doi:10.1523/JNEUROSCI.0471-20.2020 (2020).
- 32 Chen, Y. *et al.* Single-Cell Transcriptomic Profiling in Inherited Retinal Degeneration Reveals Distinct Metabolic Pathways in Rod and Cone Photoreceptors. *Int J Mol Sci* **23**, doi:10.3390/ijms232012170 (2022).
- 33 Jin, S. Q. *et al.* Inference and analysis of cell-cell communication using CellChat. *Nat Commun* **12**, doi:ARTN 1088 10.1038/s41467-021-21246-9 (2021).
- 34 Sarin, S. *et al.* Role for Wnt Signaling in Retinal Neuropil Development: Analysis via RNA-Seq and In Vivo Somatic CRISPR Mutagenesis. *Neuron* **98**, 109-126 e108, doi:10.1016/j.neuron.2018.03.004 (2018).
- 35 Shekhar, K. *et al.* Comprehensive Classification of Retinal Bipolar Neurons by Single-Cell Transcriptomics. *Cell* **166**, 1308-1323 e1330, doi:10.1016/j.cell.2016.07.054 (2016).
- 36 Dou, J. *et al.* Bi-order multimodal integration of single-cell data. *Genome Biol* **23**, 112, doi:10.1186/s13059-022-02679-x (2022).

- 37 Luhmann, U. F. *et al.* Role of the Norrie disease pseudoglioma gene in sprouting angiogenesis during development of the retinal vasculature. *Invest Ophthalmol Vis Sci* **46**, 3372-3382, doi:10.1167/iovs.05-0174 (2005).
- 38 Moscona, A. A., Fox, L., Smith, J. & Degenstein, L. Antiserum to lens antigens immunostains Muller glia cells in the neural retina. *Proc Natl Acad Sci U S A* **82**, 5570-5573, doi:10.1073/pnas.82.16.5570 (1985).
- 39 Hao, Y. H. *et al.* Integrated analysis of multimodal single-cell data. *Cell* **184**, 3573-+, doi:10.1016/j.cell.2021.04.048 (2021).
- 40 Trapnell, C. *et al.* The dynamics and regulators of cell fate decisions are revealed by pseudotemporal ordering of single cells. *Nat Biotechnol* **32**, 381-386, doi:10.1038/nbt.2859 (2014).
- 41 Andreatta, M. & Carmona, S. J. UCell: Robust and scalable single-cell gene signature scoring. *Comput Struct Biotechnol J* **19**, 3796-3798, doi:10.1016/j.csbj.2021.06.043 (2021).
- 42 Youle, R. J. & Strasser, A. The BCL-2 protein family: opposing activities that mediate cell death. *Nat Rev Mol Cell Biol* **9**, 47-59, doi:10.1038/nrm2308 (2008).
- 43 Kapoor, I., Bodo, J., Hill, B. T., Hsi, E. D. & Almasan, A. Targeting BCL-2 in B-cell malignancies and overcoming therapeutic resistance. *Cell Death Dis* **11**, 941, doi:10.1038/s41419-020-03144-y (2020).
- 44 Czabotar, P. E., Lessene, G., Strasser, A. & Adams, J. M. Control of apoptosis by the BCL-2 protein family: implications for physiology and therapy. *Nat Rev Mol Cell Biol* **15**, 49-63, doi:10.1038/nrm3722 (2014).
- 45 Klanova, M. & Klener, P. BCL-2 Proteins in Pathogenesis and Therapy of B-Cell Non-Hodgkin Lymphomas. *Cancers (Basel)* **12**, doi:10.3390/cancers12040938 (2020).
- 46 Kamimoto, K. *et al.* Dissecting cell identity via network inference and in silico gene perturbation. *Nature* **614**, 742-751, doi:10.1038/s41586-022-05688-9 (2023).
- 47 Jingjing, Z. *et al.* A novel MEF2C mutation in lymphoid neoplasm diffuse large B-cell lymphoma promotes tumorigenesis by increasing c-JUN expression. *Naunyn Schmiedebergs Arch Pharmacol* **393**, 1549-1558, doi:10.1007/s00210-019-01764-6 (2020).
- 48 Ying, C. Y. *et al.* MEF2B mutations lead to deregulated expression of the oncogene BCL6 in diffuse large B cell lymphoma. *Nat Immunol* **14**, 1084-1092, doi:10.1038/ni.2688 (2013).
- 49 Hodson, D. J. *et al.* Regulation of normal B-cell differentiation and malignant B-cell survival by OCT2. *Proc Natl Acad Sci U S A* **113**, E2039-2046, doi:10.1073/pnas.1600557113 (2016).
- 50 Yu, B. *et al.* FOXP1 expression and its clinicopathologic significance in nodal and extranodal diffuse large B-cell lymphoma. *Ann Hematol* **90**, 701-708, doi:10.1007/s00277-010-1124-9 (2011).
- 51 Brown, P. J. *et al.* FOXP1 suppresses immune response signatures and MHC class II expression in activated B-cell-like diffuse large B-cell lymphomas. *Leukemia* **30**, 605-616, doi:10.1038/leu.2015.299 (2016).

- 52 Wlodarska, I. *et al.* FOXP1, a gene highly expressed in a subset of diffuse large B-cell lymphoma, is recurrently targeted by genomic aberrations. *Leukemia* **19**, 1299-1305, doi:10.1038/sj.leu.2403813 (2005).
- 53 Gascoyne, D. M. & Banham, A. H. The significance of FOXP1 in diffuse large B-cell lymphoma. *Leuk Lymphoma* **58**, 1037-1051, doi:10.1080/10428194.2016.1228932 (2017).
- 54 Wu, T. *et al.* The TCF1-Bcl6 axis counteracts type I interferon to repress exhaustion and maintain T cell stemness. *Sci Immunol* **1**, doi:10.1126/sciimmunol.aai8593 (2016).
- 55 Butler, A., Hoffman, P., Smibert, P., Papalexi, E. & Satija, R. Integrating single-cell transcriptomic data across different conditions, technologies, and species. *Nature Biotechnology* **36**, 411+, doi:10.1038/nbt.4096 (2018).
- 56 Wang, C. F. *et al.* Integrative analyses of single-cell transcriptome and regulome using MAESTRO. *Genome Biology* **21**, doi:ARTN 198 10.1186/s13059-020-02116-x (2020).
- 57 Korsunsky, I. *et al.* Fast, sensitive and accurate integration of single-cell data with Harmony. *Nature Methods* **16**, 1289+, doi:10.1038/s41592-019-0619-0 (2019).